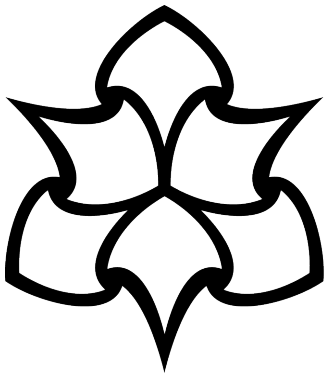

JOURNAL OF MATERIALS RESEARCH AND TECHNOLOGY 2022;21:576–589

Available online at www.sciencedirect.com

jmr&t Journal of Materials Research and Technology

journal homepage: www.elsevier.com/locate/jmrt

Original Article

Tailoring the corrosion and tribological performance of Ti-modified MoS_2-based films in simulated seawater

Xiangru Shi [a,*], *Peihua He* [a], *Shangqi Sun* [b,**], *Jian Chen* [b], *Ben D. Beake* [c], *Tomasz W. Liskiewicz* [d], *Xin Zhang* [a], *Zehua Zhou* [a]

[a] *College of Mechanics and Materials, Hohai University, Nanjing 210098, China*

[b] *School of Materials Science and Engineering, Jiangsu Key Laboratory for Advanced Metallic Materials, Southeast University, Nanjing 211189, China*

[c] *Micro Materials Ltd., Willow House, Yale Business Village, Ellice Way, Wrexham, LL13 7YL, UK*

[d] *Faculty of Science and Engineering, Manchester Metropolitan University, John Dalton Building, Charles Street, Manchester M15 6BH, UK*

ARTICLE INFO

Article history:
Received 20 June 2022
Accepted 14 September 2022
Available online 21 September 2022

Keywords:
Ti-modified MoS_2 film
Tribological properties
Corrosion resistance
Aggressive environment

ABSTRACT

Film protection has become a crucial means to improve the corrosion and wear performance of key components in aggressive environment. In this study, the feasibility of using MoS_2-based modified films in artificial seawater (3.5% NaCl solution) was evaluated by co-deposition of Ti to produce Ti–MoS_2 composite and Ti/MoS_2 multilayer films. The microstructure, wettability, mechanical, tribological and corrosion behavior of the Ti-modified MoS_2-based films was contrasted to pure MoS_2 film. The results show that the incorporation of Ti not only improves densification, but also promotes a transformation from a columnar to an amorphous film structure, leading to the improvement of mechanical properties of Ti–MoS_2 composite film and Ti/MoS_2 multilayer film. The friction coefficient curves of all of the three MoS_2-based film in 3.5 wt% NaCl solution show stable values during the sliding process. The advantage of the preferential (002) growth orientation, improved mechanical properties and reduced hydrophobicity for both of the Ti-modified MoS_2 films caused the decreased friction coefficient and wear rate in NaCl solution. The electrochemical results before and after friction show that the ranking of corrosion resistance is Ti/MoS_2 multilayer > Ti–MoS_2 composite film > pure MoS_2 film, which is attributed to the compact microstructure and the presence of surface passive films.

* Corresponding author.
** Corresponding author.
E-mail addresses: sxr12009210@163.com (X. Shi), sunsq0805@hotmail.com (S. Sun).

https://doi.org/10.1016/j.jmrt.2022.09.061

1. Introduction

With the rapid development of modern industry, environmental protection and long-term service of engineering equipment became more changeable and demanding. For example, when ocean platforms, steamships, offshore oil and gas field equipment and other facilities are in service in seawater environment, their key components such as bearings, valves, and sealing rings not only face the mechanical damage caused by external loading, but also often are subjected to simultaneous corrosive degradation in seawater medium, causing the rapid failure of metal components and unnecessary economic losses [1–4]. Therefore, the development of high-performance wear-resistant and anti-corrosion film materials and the exploration of their corrosion and wear mechanism in harsh environment have become one of the research hotspots in the field of surface engineering and new materials [5–7].

Recently, transition metal dichalcogenide (TMD) films such as MoS_2, have attracted extensive attention from researchers in various applications due to their desirable wear and corrosion resistance, and suitability for operation in environments (*e.g.* space) where conventional liquid lubrication is impossible [8–11]. MoS_2 films are composed of sandwich lamellar structure with high mechanical strength, good wear resistance, environmental protection and low pollution, which make them potential applications in aerospace, metal processing and automobile industry to replace current coating solutions for environmental reasons (*e.g.* growing legislation to replace Cr^{6+}) [12–15]. However, the serious environmental sensitivity of MoS_2 films restrict their applications in complex service condition. When the MoS_2 films operate in humid environment, the H_2O and O_2 can easily captured by high-energy dangling bonds on the surface to produce compounds such as H_2SO_4 and MoO_3, respectively [16–18]. The relatively hard MoO_3 particles will greatly increase the friction coefficient of the film, while the strong acid H_2SO_4 will aggravate the corrosion damage of the film.

Among various modification methods, elemental doping has been the most commonly used and effective way to regulate the microstructure and tribological performance of MoS_2 films for industrial applications [18–22]. For example, *Hudec* et al. [21] found with N-doping Mo–S–N films showed either an amorphous structure or a composite structure of amorphous and nanocrystalline regions, which greatly improved the hardness and wear resistance in humid air compared with the undoped one. *Xu* et al. [20] reported that the introduction of Si element could not only improve the porous columnar structure of MoS_2 films to produce a compact featureless morphology, but also capture the O_2 in ambient air, resulting in the enhancement of tribological properties. In addition to the non-metallic elements, the doping of metallic elements can also inhibit the oxidation reaction of MoS_2 by preferential oxidation. *Zhang* et al. [23] showed that the silver molybdate can be produced when Ag element is combined with MoS_2 film, which weakened and prevented the reaction of MoS_2 and effectively reduced the friction coefficient of the composite film in humid environment. *Zeng* et al. [18] indicated W-doped MoS_2 films maintain lower temperature-sensitivity and better tribology performance in the atmospheric environment attributing to the improved mechanical properties and preferred growth orientation of the (002) basal plane. Nevertheless, metal Ti-doped MoS_2 composite films have attracted much attention due to their denser structure and better oxidation resistance than other doped composite films [8,17,24,25]. The introduction of Ti can not only change the structure of the MoS_2 into a more disordered state and improve the density, but also preferentially combine with oxygen to form a dense TiO_2 surface layer, which prevents the further diffusion and migration of atomic oxygen to the interior of the film, thereby exerting a protective effect on the whole film.

Alongside this, in recent years multilayer structure design has been another effective research strategy to improve the oxidation resistance and tribological performance of MoS_2 films [16,26–28]. When the second phase is introduced into MoS_2 film to form a nano-multilayered structure, the stress state and microstructure defects of the film can be effectively improved. The interface effect of multilayer structure can prevent large-area peeling and crack propagation of the film during frictional sliding, and effectively block the diffusion path of corrosive media such as water molecules and oxygen in the film, improving the tribological properties of the films in humid environment. *Zeng* et al. [26] prepared multilayer film with compact structure and favorable (002) plane growth orientation by combing two TMDs of MoS_2 and WS_2. It was found the MoS_2/WS_2 multilayer film exhibited better tribological properties and corrosion resistance than the composite film as the interfacial effect improved the film hardness and hindered the diffusion of corrosive medium. Similarly, the multilayer structure formed by the alternating deposition of MoS_2 and Ti can also effectively inhibit the growth of the columnar structure of the film and increase the density of the film, thus reducing the friction coefficient and improving the wear resistance of the films. *Li* et al. [8] reported the Pb–Ti/MoS_2 nanoscaled multilayer films exhibited excellent mechanical and tribological properties than pure MoS_2 resulting from the high basal plane oriented growth of film structure. The results from *Sun* et al. [16] showed the improved adhesion strength and the construction of multilayer structure promoted the Ti–MoS_2/Ti multilayer film to have lower friction coefficient and longer friction life under atmospheric environment.

However, most of studies to date have only explored the tribological properties of MoS_2-based composite films in vacuum or atmospheric environment, ignoring the effect of corrosive medium. The tribological properties of MoS_2-based films in corrosion solution are still far less understood, and the wear mechanism is not clear. In particular, there is almost no research on the corrosion resistance of MoS_2-based films before and after tribological experiments.

In this study, Ti–MoS_2 composite film and Ti/MoS_2 multilayer film were deposited on 304 stainless steel by unbalanced magnetron sputtering. The microstructure, mechanical properties, tribological performance and corrosive resistance were systematically investigated and compared with the pure MoS_2 film. The tribological experiments were conducted in simulated seawater, while the corrosion resistance was assessed before and after the tribological experiments. The preliminary results obtained will act as a baseline to aid the

ultimate development and utilization of high-performance MoS_2-based films for applications in aggressive corrosive environments.

2. Experimental section

2.1. Film preparation

The closed field unbalanced magnetron sputtering system (CF-800, Teer Coating Ltd., UK) was used to deposit pure MoS_2 films, Ti–MoS_2 composite films and Ti/MoS_2 multilayer films on the mirror-polished 304 stainless steel. Before deposition, the steel substrates were ultrasonically cleaned in acetone and ethanol for 20 min, separately, and then fixed in the vacuum chamber with two Ti targets (purity 99.99%) and two MoS_2 targets (purity 99.99%) positioned symmetrically. After the chamber pressure was pumped down to below 1.0×10^{-3} Pa, the working gas Ar was introduced to remove the surface oxide contamination with a bias voltage of −500 V for 30 min. After that, a Ti bonding layer was produced on the substrate surfaces at 3 A Ti target current and −70 V bias voltage to improve the adhesion strength between the substrate and film. Finally, the Ti-modified MoS_2-based films were deposited with the Ti target current of 1.4 A and MoS_2 target current of 2 A by changing the rotation rate of the sample holder. For the Ti–MoS_2 composite film, the rotation rate of sample holder was set to 10 r/min to make Ti uniformly distributed in the MoS_2 matrix, while the rotation rate of 3 r/min was used to produce different nanolayers for the Ti/MoS_2 multilayer film. A pure MoS_2 film was also deposited with the MoS_2 target current of 2 A.

2.2. General characterization

The crystalline structure of the films was determined in the 2θ range of 5–80° by X-ray diffraction (XRD, D8-Discover, Bruker Co., Germany) with Cu Kα ray. The surface and cross-sectional morphologies of the films were observed by scanning electron microscopy (SEM, XL-30, FEI Co., USA) at 20.0 KV, with energy dispersive spectroscopy (EDS) used to analyze the elemental distribution in the films. Surface roughness and morphology of the films was assessed by atomic force microscopy (AFM, Bruker Co., Germany) with an imaging area of $2 \times 2\ \mu m^2$. The microstructure of the Ti–MoS_2 composite films and Ti/MoS_2 multilayer films were also characterized by a high-resolution transmission electron microscopy (HRTEM, Tecnai F20, FEI Co., USA). The TEM samples were prepared by a focused ion beam (FIB, Strata 400S, FEI Co., USA). Raman spectroscopy (Alpha300R, WITec Co., Germany) was used to analyze the characteristic peaks of MoS_2 by using an Ar^+ laser of 532 nm in the range of 200–500 cm^{-1}. X-ray photoelectron spectroscopy (XPS, Thermo Scientific K-Alpha, Thermo-Fisher Co., USA) was performed to measure the element and bonding state of the films with monochromatic AlKα irradiation.

2.3. Mechanical and wettability testing

The hardness (*H*) and elastic modulus (*E*) of the films were measured by a calibrated nanoindentation system (IMicronanoindenter, Nanomechanics Inc., USA) in continuous stiffness mode with a Berkovich diamond indenter. The maximum indentation depth was set to 200 nm less than 10% of the film thickness to minimize the effect of underlying substrate as much as possible. Each sample was retested 10 times to mitigate the effect of surface roughness and defects in the films. Contact angle measurement on the films surface were performed at room temperature by using a drop shape analysis system (JC2000D1, POWEREACH, China). The droplet of the deionized water placed on the sample surface is 3.0 μL. Three repeated tests were carried out at different positions on the sample surface to obtain the average value of water contact angle to eliminate errors.

2.4. Tribological and corrosion testing

The tribological experiments were conducted with a ball-on-disc rotary tribometer in 3.5 wt% NaCl solution. ZrO_2 ceramic balls with a diameter of 5 mm were chosen as the counterparts due to their high hardness, good wear resistance and potential application in water-lubricated components as bearing and mechanical seals [29]. The applied load, rotation speed and radius were 5 N, 180 r/min, and 4 mm, respectively. Each test was repeated three times with a single test time of 35 min. The wear morphology on the films and the wear scars on the ZrO_2 balls were observed by optical microscopy (OM, MV3000, Jiangnan Novel Optics Co., China) and SEM (SN3400, Hitachi, Japan). The specific wear rate was calculated by the cross-sectional profiles of the wear track obtained by the white light interferometer (HST-200, RTEC, USA).

The electrochemical experiments of the films were evaluated by using CHI660E electrochemical setup (CH Instruments Ins. USA) with an active area of 1 cm^2. The potentiodynamic polarization and electrochemical impendence spectroscopy (EIS) were obtained in 3.5 wt% NaCl solution before and after the tribological testing. The three electrode cell was composed of the films as the working electrode, an Ag/AgCl electrode as the reference electrode, a platinum sheet as the counter electrode. The stable open circuit potentials (OCP) were obtained after the samples were immersed in 3.5 wt% NaCl solution for 30 min. The range of scanning potential for the potentiodynamic polarization curve was set from −1 V to 1.5 V at a scanning rate of 0.5 mV/s. The EIS tests were conducted at the frequency ranged from 0.01 Hz to 100 kHz. Each sample was tested twice to verify the data repeatability.

3. Results and discussion

3.1. Composition and morphology of MoS_2-based films

The composition of the three as-deposited films by EDS is shown in Table 1. The data in the table refer to the atomic percentage of each element in the films, where the total compositions were normalized to 100 at.%. The atomic content of Ti element is about 8.63% and 8.23% for Ti–MoS_2 composite film and Ti/MoS_2 multilayer film, separately, while no Ti element was detected in the pure MoS_2 film despite of the presence of Ti adhesion layer. The S/Mo atomic ratio is in the range of 1.80–1.92 for the three films, which is a little less

Table 1 – The composition of the as-deposited films.

Samples	Mo (at. %)	S (at. %)	Ti (at. %)	O (at. %)	S/Mo
Pure MoS_2 film	32.70 ± 0.77	62.87 ± 0.66	/	4.44 ± 0.96	1.92 ± 0.05
Ti–MoS_2 composite film	31.92 ± 0.48	57.51 ± 1.41	8.63 ± 0.22	1.95 ± 0.59	1.80 ± 0.07
Ti/MoS_2 multilayer film	31.62 ± 0.53	59.07 ± 0.46	8.23 ± 0.22	1.09 ± 0.89	1.87 ± 0.03

than that of the ideal stoichiometric MoS_2. The reason could be attributed to the reverse sputtering effect of S element caused by high-energy particle etching [30,31]. Moreover, the activation of Ti targets would increase the energy of the bombarding particles, leading to more deficiency of S atoms in modified MoS_2-based films than pure MoS_2 film. The presence of O element in the films is mainly attributed to the residual oxygen in the vacuum chamber and the adsorbed oxygen on the surface of testing samples. The detailed difference will be discussed later.

The surface, cross-sectional SEM morphologies and the corresponding three-dimensional AFM topographies of the three as-deposited films are shown in Fig. 1. It can be seen the surface of the pure MoS_2 film showed typically cauliflower-like structure composed of aggregated particles. Obvious micro-pores and defects can be observed in the boundary of the uneven mastoid structure. Although a similar 'island-like' appearance is also observed on the surface of Ti–MoS_2 composite film and Ti/MoS_2 multilayer film, the stacked particles are more uniform and denser with smaller size and fewer defects. The cross-sectional morphologies in middle of Fig. 1 show that the undoped MoS_2 film is loose and porous, exhibiting typical columnar morphology, while the Ti–MoS_2 composite film and Ti/MoS_2 multilayer film display a more featureless orientation and compact microstructure. The total thickness of the three films is basically the same in the range of 2.15 ± 0.05 μm. Consistent with the SEM results, the AFM topographies also confirmed that the modified MoS_2-based films exhibit more smooth and compact island structure than the pure MoS_2 film. The R_a surface roughness is 8.94 nm, 4.51 nm and 5.14 nm for the pure MoS_2 film, Ti–MoS_2 composite film and Ti/MoS_2 multilayer film, respectively.

According to the island growth model of MoS_2 films [26], the sputtered adatoms could nucleate by colliding with each other in the deposition process. The absence of high-energy atomic bombardment of the last layer atoms leads to the formation of cauliflower-like structure. For the Ti–MoS_2 composite film, the introduction of metal Ti could react preferentially with residual O in the chamer to form TiO_x, which could act as a nucleation barrier to suppress the formation of MoS_2 columnar crystal structure [32]. Similarly, the growth of columnar crystal structure for Ti/MoS_2 multilayer film could abruptly interrupted by alternately deposited metal layers, which can effectively reduce the defects and porosity through the film thickness. These result in their more uniform and compact surface and cross-sectional morphologies than the pure MoS_2 film, so that they can play a positive role in blocking the invasion of water and oxygen in the marine environment and pledge the production life.

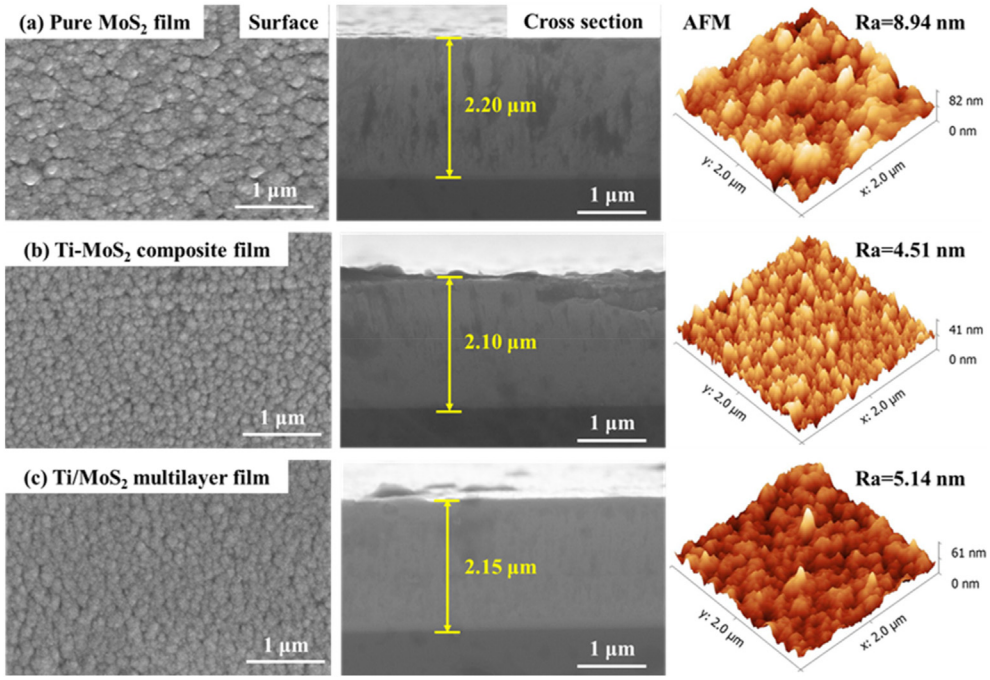

Fig. 1 – The SEM surface, cross-sectional morphologies and AFM surface topographies of the films: (a) pure MoS_2 film, (b) Ti–MoS_2 composite film, and (c) Ti/MoS_2 multilayer film.

3.2. Crystal structure and bonding state of MoS_2-based films

The XRD patterns were obtained to analyze the crystal structure of the three as-deposited films, as shown in Fig. 2a. Besides the diffraction peaks from the substrate, two peaks around $2\theta = 33^\circ$ and 59° were observed for the pure MoS_2 film, which are coming from the MoS_2 (100) and (110) crystal planes respectively. However, the addition of metal Ti led to the disappearance of the (100) and (110) diffraction peaks. Instead, a new diffraction peak at around $2\theta = 13^\circ$ appeared in the film of Ti–MoS_2 composite film and Ti/MoS_2 multilayer film, corresponding to the MoS_2 (002) basal orientation. Compared with the evident diffraction peaks of pure MoS_2 film, the diffraction peaks of Ti–MoS_2 composite film and Ti/MoS_2 multilayer film were weaker and broader, indicating the phase structure transformation from columnar crystal to amorphous structure. This fact could be caused by the lattice distortion due to the incorporation of metal Ti [25]. Besides, the Ti/MoS_2 multilayer film showed a stronger (002) diffraction peak than the Ti–MoS_2 composite film, suggesting that the periodic multilayer structure is favorable to the growth of MoS_2 (002) basal orientation. Moser et al. [33] pointed that the structure of MoS_2 film near the interface is (002) planes parallel with the substrate in the first growth stage, and then develops to the orientation perpendicular to the substrate. The alternately deposited Ti nanolayers could interrupt the growth of the film perpendicular to the substrate. In addition, it should be noted that due to the relatively low element content, no Ti diffraction peak is detected in the XRD pattern of the Ti-modified MoS_2-based films.

In order to deeper understand the microstructure of the as-deposited films, Raman spectra were collected in the range of 300–500 cm^{-1}. As shown in Fig. 2b, there are two typical characteristic peaks located at around 375 and 410 cm^{-1}, corresponding to the E_{2g} and A_{1g} vibrational modes of Raman spectra for all of the three films. Compared to the pure MoS_2 film, the characteristic peak intensity of the Ti-modified MoS_2-based films decreases dramatically, indicating that the crystallization of the films decreased [21,34]. This fact coincides with XRD results.

The chemical bonds of the three as-deposited films are characterized by XPS, in which the Mo 3d, S 2p, and O 1s spectra were fitted by Guassian-Lorentian function shown in Fig. 3. For Mo 3d, three different bonding states are observed for all of the three films. The peaks located at around 230.8 eV and 232.5 eV are referring to the Mo $3d_{5/2}$ and Mo $3d_{3/2}$ for MoS_2 [26,35,36]. Meanwhile, the peaks of Mo $3d_{5/2}$ and Mo $3d_{3/2}$ belonging to MoS_{2-x} are observed at around 229.1 eV and 232.1 eV, which could explain the EDS result of S/Mo atomic ratio below stoichiometric value of 2 [37]. In addition, there are two high-energy peaks located at around 232.9 eV and 235.5 eV, assigned to MoO_3 [38]. It can be observed that the percentage of MoO_3 peak area of Ti-modified MoS_2 films is obviously lower than the pure MoS_2. Based the fitting results, the percentage of MoO_3 peak area is 11.23%, 5.69% and 2.51% for pure MoS_2 film, Ti–MoS_2 composite film and Ti/MoS_2 multilayer film, respectively. To verify this result, the XPS peaks of O 1s for the three films were fitted to two different peaks of surface oxygen and lattice oxygen, at around 532.1 eV and 532.8 eV [19]. The former is caused by the adsorption of oxygen atoms on the samples surface, while the latter is formed by the reaction of the metal (Mo, Ti etc.) with residual oxygen in the chamber. Similarly, the lattice oxygen in the Ti-modified MoS_2 films is lower than that in pure MoS_2 film. This indicates that the addition of Ti inhibits the oxidation of MoS_2, and the multilayer structure is more effective in keeping oxygen out of films. The S 2p peaks were also fitted to provide more insight to the film structure. The doublet peaks at around 161.9 eV and 163.2 are referred to the S $2p_{3/2}$ and S $2p_{1/2}$ of MoS_{2-x}, while the other doublet peaks of MoS_2 locate at around 162.1 eV and 164.3 eV, respectively, consistent with the analysis of Mo 3d spectrum [38]. For the Ti 2p spectrum, there were no obvious peaks of both the Ti–MoS_2 composite film and Ti/MoS_2 multilayer film due to the trace concentration of Ti and the low signal/noise ratio. However, it still can be distinguished there are two peaks at about 458.5 eV and 464.9 correspond to Ti $2p_{3/2}$ and Ti $2p_{1/2}$ in TiO_2 [24], which evidenced the oxygen trapping ability of Ti element in humid environment.

FIB/TEM was used to further analyze the crystal structure of the Ti–MoS_2 composite film and Ti/MoS_2 multilayer film. As shown by the High-Angle Annular Dark Field (HAADF) image in Fig. 4a, large amounts of bright Ti stripes are evenly distributed in the dark MoS_2 matrix for the Ti–MoS_2 composite film, which is consistent with the morphology of previous reported MoS_2/Pb–Ti composite film [27]. The selected area electron diffraction (SAED) pattern in the inset of Fig. 4a indicates the weak crystallinity of the Ti–MoS_2 composite film. The high-resolution TEM (HR-TEM) image in Fig. 4b demonstrates the quasi-amorphous structure with short-distance ordered nanocrystalline regions. The measured d-spacing of about 0.612 nm confirmed the (002) crystal plane of the grains. Although some growth is parallel to the substrate, the (002) crystal planes oriented randomly as a whole in the Ti–MoS_2 composite film. According to HAADF image in Fig. 4c, the Ti/MoS_2 multilayer film displays a distinct alternating light and shade multilayer structure, corresponding to the Ti and MoS_2 layer, respectively. The SAED pattern in the insert shows the same diffraction halo with the Ti–MoS_2 composite film, indicating the nanocrystalline/amorphous composite structure. The HRTEM also shows the classic sandwich structure, where the Ti layer is sandwiched by two MoS_2 layers. The thickness of Ti/MoS_2 bilayer is about 10 nm, including 6 nm of MoS_2 and 4 nm of Ti layer. Different to the disordered arrangement of (002) crystal plane in Ti–MoS_2 composite film, most of that in Ti/MoS2 film is parallel to the substrate, which could be attributed to the blocking effect of the film perpendicular to the substrate by the periodic nanostructure [26]. This result is consistent with the XRD analysis. Besides, Fig. 4e shows the mapping scanning of the Ti/MoS_2 multilayer film in HADDF mode to distinguish the element distribution. It can be observed that the stratification of Mo and Ti element is obvious, which is corresponded to the dark and while region, respectively. The S element diffused throughout the whole cross section.

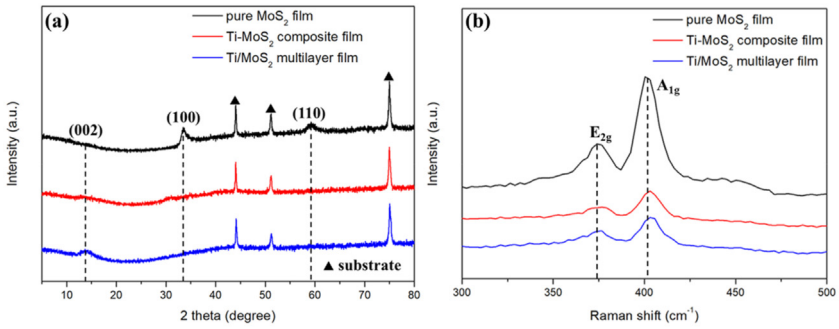

Fig. 2 – (a) XRD and (b) Raman spectra of the as-deposited films.

3.3. *Mechanical and hydrophobic properties of MoS_2-based films*

The mechanical properties of MoS_2-based films play an important role in influencing their tribological properties, with high hardness generally corresponds to improved wear resistance [39,40]. Fig. 5 shows the hardness (*H*) and elastic modulus (*E*) of the three as-deposited films. It can be seen the hardness of Ti–MoS_2 composite film is about 10.2 GPa, which is over three times higher than the pure MoS_2. Compared with the composite film, the hardness of Ti/MoS_2 multilayer film decreased slightly to about 9.3 GPa. The elastic modulus is about 74 GPa, 130 GPa, and 118 GPa for the pure MoS_2 film, Ti–MoS_2 composite film and Ti/MoS_2 multilayer film, respectively. The nanocrystalline/amorphous composite structure should be the most important reason for the improved mechanical properties of Ti-modified MoS_2-based films, which improved significantly the densification of the films shown in Fig. 1. Besides, the transformation to an amorphous structure could reduce the dislocation and inhibit dislocation movement in films structure, which is also beneficial for the improved hardness [17,28]. The H/E and H^3/E^2 ratios can also correlate with wear resistance. The former is an indicator of the elastic strain to failure and resilience of hard films, while the latter is related to their resistance to plastic deformation [41,42]. The insert table in Fig. 5 show markedly higher H/E and H^3/E^2 value of Ti-modified MoS_2 than that of pure MoS_2 film. Compared to the composite film, the H/E of Ti/MoS_2 multilayer film is a little higher.

Besides the mechanical properties, the wettability behavior is also generally required for some specific applications in conjunction with their good corrosion and wear resistance, especially in the marine environment. To evaluate the wettability of the three as-deposited films, the water

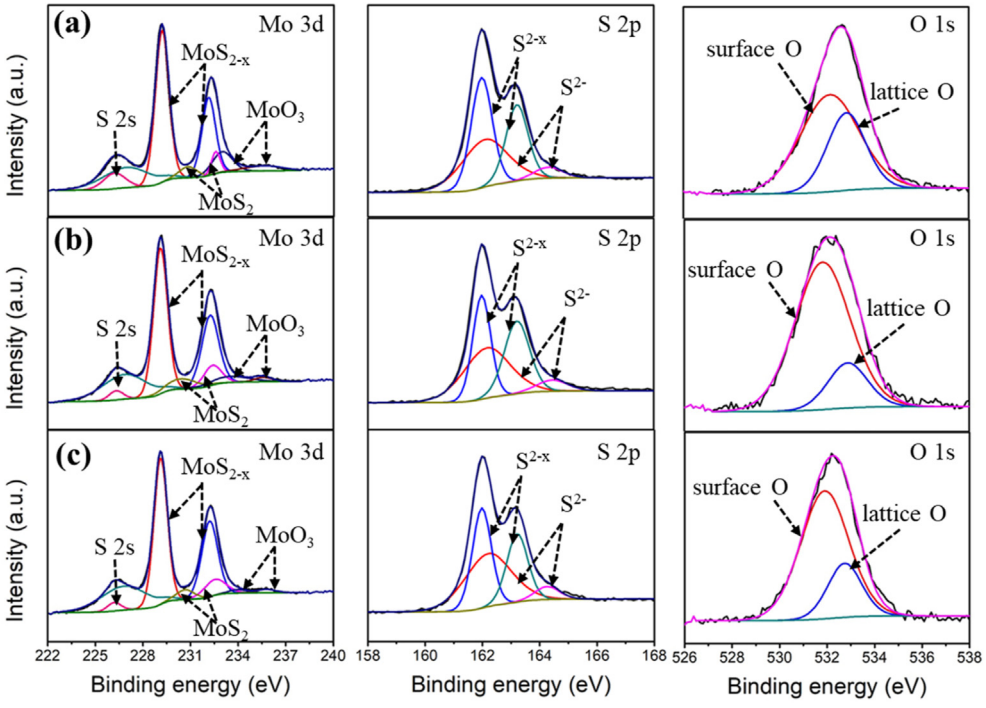

Fig. 3 – Mo 3d, S 2p and O 1s decomposition of XPS spectra for the films: (a) pure MoS_2 film, (b) Ti–MoS_2 composite film, and (c) Ti/MoS_2 multilayer film.

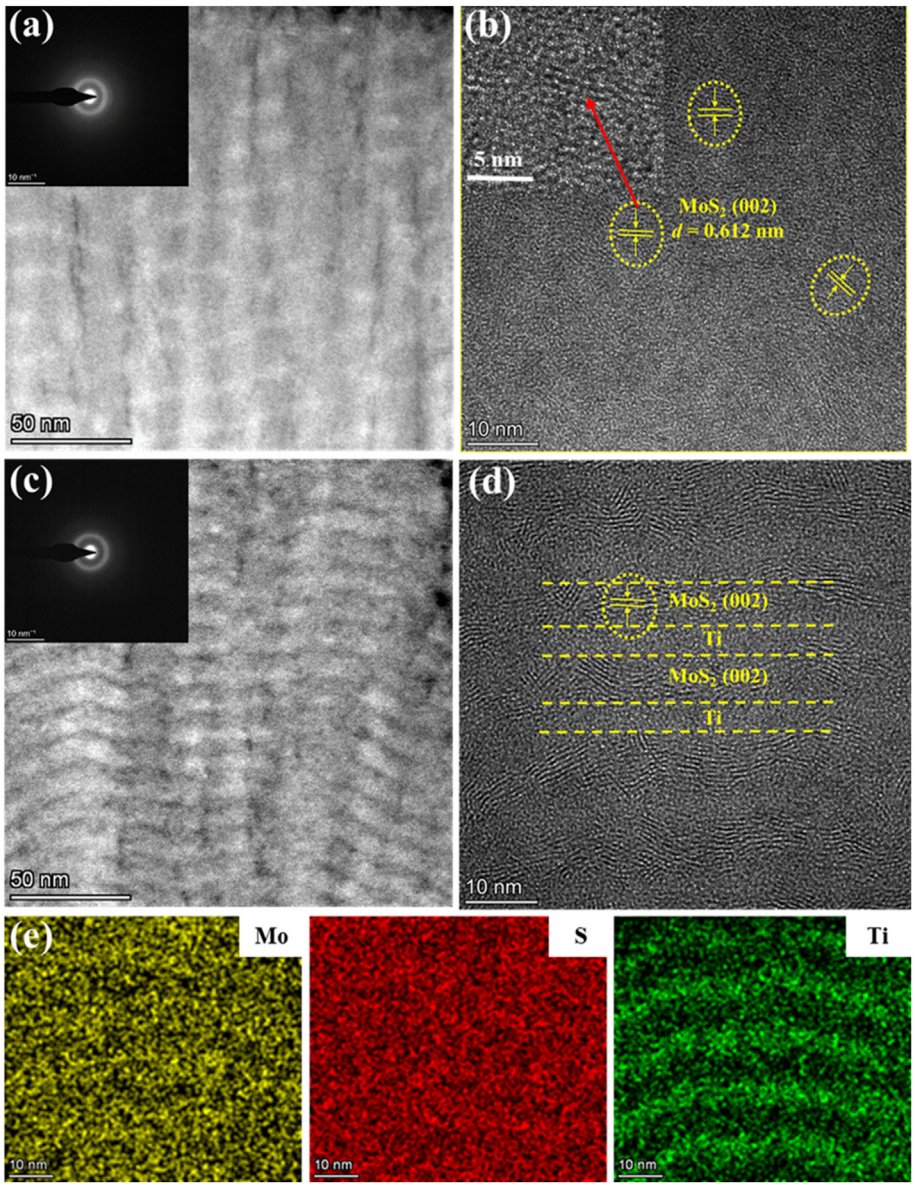

Fig. 4 – (a) HAADF, (b) HR-TEM image of Ti–MoS2 composite film, (c) HAADF, (d) HR-TEM image, and (e) the selected area mapping of Ti/MoS_2 multilayer film.

contact angle (WCA) was measured by using a high-speed camera, as shown in Fig. 6. It can be seen the MoS_2 film surface is hydrophobic with a WCA of approximately 96.2°. However, the introduction of Ti resulted in the formation of a slightly more hydrophilic surface, with WCAs of about 85.6° and 83.4° for the Ti–MoS_2 composite film and Ti/MoS_2 multilayer film, respectively. It is known the surface wettability is influenced by the chemical composition, surface roughness and surface contaminant [43]. The chemical composition determines the surface energy of the material, which plays a crucial role in evaluating the wettability of solid surface. As reported in previous studies [22,44,45], MoS_2 film is a nonpolar material with low surface energy, which is supposed to be responsible for the hydrophobic surface. The incorporation of Ti could improve the surface energy of modified MoS_2 films, resulting in the enhancement of wettability observed. Besides, the surface roughness and morphology should be also related to the wettability of the films. Based on Wenzel's equation: $\cos\theta^* = r\cos\theta$ (r is the roughness ratio, θ^* and θ is the apparent contact angle and young contact angle, respectively) [43], when the contact angle is greater than 90°, the hydrophobicity of the film increases with the increase of surface roughness. Conversely, it decreases with the increases of surface roughness. Shown in the AFM topography of Fig. 1, the high surface roughness of the pure MoS_2 film could be beneficial to the hydrophobic properties of the film. The decreased WCA of the Ti-modified MoS_2-based film could be attributed to the disappearance of the cauliflower-like microstructure. Moreover, the porous surface could increase the adsorption of hydrocarbons onto the surface of the MoS_2 film, which could also reinforce the hydrophobic behavior [22,44].

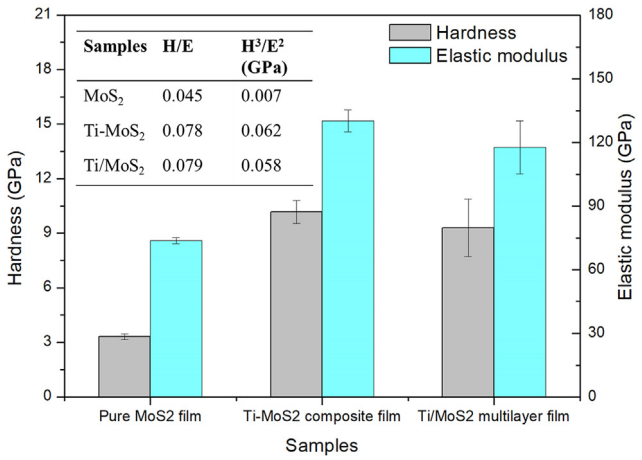

Fig. 5 – Hardness (*H*) and elastic modulus (*E*) of the as-deposited films (The insert is the table of *H/E* and H^3/E^2).

3.4. *Tribological properties of MoS_2-based films in 3.5 wt.% NaCl solution*

Fig. 7 shows the friction coefficient curves of the pure MoS_2 film and Ti-modified MoS_2 films as a function of sliding time in 3.5 wt% NaCl solution. After a short running-in period, the friction coefficient of pure MoS_2 film increases rapidly to a relatively stable value of about 0.055. The slight fluctuation of the friction curve could be caused by the vibration of the rotating sample stage. Differently, the friction curves of both the Ti-modified MoS_2-based films experienced a rapid decline process to the sable value after the running-in period. It can be seen the stable friction coefficient of the Ti–MoS_2 composite film and Ti/MoS_2 multilayer film is basically almost identical and are significantly lower than the MoS_2 film. Fig. 8 shows the corresponding specific wear rate of the three as-deposited films in NaCl solution. The pure MoS_2 film presents the highest wear rate of about 9.09×10^{-6} mm^3/N m, while the wear rate is approximately 7.55×10^{-6} mm^3/N m and 7.54×10^{-6} mm^3/N m for Ti–MoS_2 composite film and Ti/MoS_2 multilayer film, respectively.

To investigate the wear mechanism of the MoS_2-based films in NaCl solution, the surface morphologies of the wear track and the corresponding wear scar on the mating balls were observed by SEM and OM, respectively. As shown in Fig. 9, the wear track of the pure MoS_2 film is relatively smooth, yet extensive ploughing grooves appear in the worn surface, indicating significant abrasive wear. Besides, a large amount of wear debris could be found stacked around the wear track for the MoS_2 film. For both the Ti-modified MoS_2 films, the ploughing grooves decrease significantly, instead there is film peeling occurred at the edge of the wear trace without wear debris accumulation. The cross-sectional profiles of the wear tracks perpendicular to the friction direction shows the depth of the wear track, as well as the width, declined with the introduction of Ti element. The optical images of the wear scar on the mating balls indicate that there is almost no transfer film on the mating ball corresponding to the pure MoS_2 film except for a large amount of debris around the wear scar. In contrast, a clear transfer film surrounding by the debris is observed in the middle area of the wear scar for the Ti-modified composite and multilayer films.

As noted previously, the tribological performance of MoS_2-based films is related to their microstructure, composition and mechanical properties. Muratore and Voevodin proposed [46] that the preferred (002) orientation of MoS_2 film exhibits better tribological performance than that of (100) orientation, attributing to the easier shear of the oriented basal planes and less chemical interaction of the sliding contacts. The XRD and TEM results in Figs. 2 and 4 demonstrated that the dominant growth orientation of Ti-modified MoS_2-based films is the MoS_2 (002) crystal plane parallel to the films surface, which did not only make the microstructure more compact to reduce the active sites of oxygen, but also make the surface easier to shear in the sliding direction. Comparatively, the columnar (100) and (110) crystal planes of pure MoS_2 film exhibited more micro-pores and defects, which are sensitive to the oxygen in the environment and react to produce the oxide particles of molybdenum (*e.g.* MoO_3, $FeMoO_4$). The hard particles give rise to the serious abrasive wear on the film surface and the damage of the transfer film on the surface of the matting ball due to the local stress concentration under the applied normal load, which resulted in the high friction coefficient and wear rate. In contrast, the doped metal Ti could react preferentially with oxygen to prevent the oxidation of molybdenum with the dense microstructure of Ti-modified MoS_2 film, which seems to be beneficial for the formation of transfer films, leading to low friction coefficient and wear rate.

The different mechanical properties of the films may also influence their tribological properties. The higher H^3/E^2 of the Ti-modified MoS_2-based films provides more load support to resist the plastic deformation of the film/substrate system, which result in the decrease of the width and depth of the wear trace [47,48]. The reduced contact area led to lower friction and wear. However, it should be noted that the

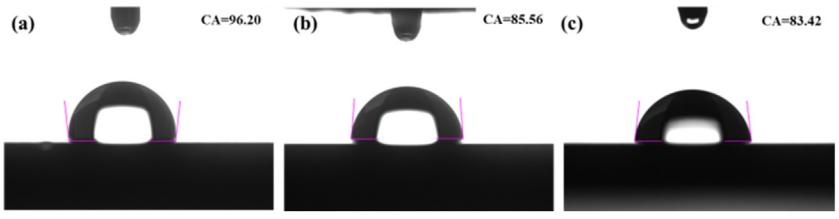

Fig. 6 – Surface contact angles of the as-deposited films with water: (a) pure MoS_2 film, (b) Ti–MoS_2 composite film, and (c) Ti/MoS_2 multilayer film.

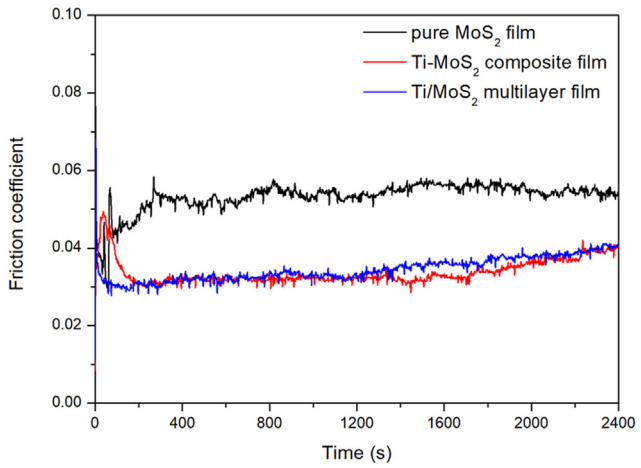

Fig. 7 – Friction coefficient curves of the three as-deposited MoS_2-based film in NaCl solution.

significant difference in elastoplastic properties between the Ti-modified MoS_2 films and stainless steel caused the film exfoliation at the edge of the wear trace after the unloading of the normal load. To mitigate this type of egg-shell effect, pre-treatment of the stainless steel (*e.g.* S-phase, plasma nitriding etc) should be done to increase the load support in the further work. Moreover, the various wettability behavior of the films could also influence their tribological performance in NaCl solution. Compared to the literature studied in vacuum or atmosphere environment [17,28], the friction coefficient of the MoS_2-based films in NaCl solution seems to be lower. This result could be attributed to the effect of water lubrication. The contact point in the hydrophilic Ti-modified MoS_2-based films is more lubricated than the hydrophobic pure MoS_2 film, leading to the better tribological performance.

3.5. *Corrosion properties of MoS_2-based films in NaCl solution*

In order to investigate the corrosion resistance of the MoS_2-based films, the potentiodynamic polarization curves of the pure MoS_2 film. Ti–MoS_2 composite film and Ti/MoS_2 multilayer film were obtained before and after friction tests in 3.5 wt% NaCl solution, as shown in Fig. 10. According to the Tafel fitting of the polarization curves, the corresponding corrosion potential (E_{corr}) and corrosion current density (I_{corr}) of the samples are summarized in Table 2. Compared with the pure MoS_2 film, the Ti-modified MoS_2-based films show a pronounced positive shift in corrosion potential, indicating improved corrosion resistance of the Ti-modified MoS_2-based films [49,50]. The corrosion potential of Ti/MoS_2 multilayer film is approximately −0.26 V, which is a little higher than −0.31 V of Ti–MoS_2 composite film. The value of I_{corr} is also an important index to evaluate the corrosion properties of materials, with lower values generally indicative of better corrosion resistance [1]. It can be seen the I_{corr} is 3.77×10^{-6} A/cm^2, 2.54×10^{-6} A/cm^2, and 1.46×10^{-6} A/cm^2 for the pure MoS_2 film, Ti–MoS_2 composite film and Ti/MoS_2 multilayer film, respectively, showing the improved corrosion resistance for the Ti/MoS_2 multilayer film. The polarization resistance (R_p) is commonly used to comprehensively judge the corrosion resistance of protective films, which is calculated bases on the I_{corr}, the anodic Tafel slope (b_a) and cathodic Tafel slope (b_c)

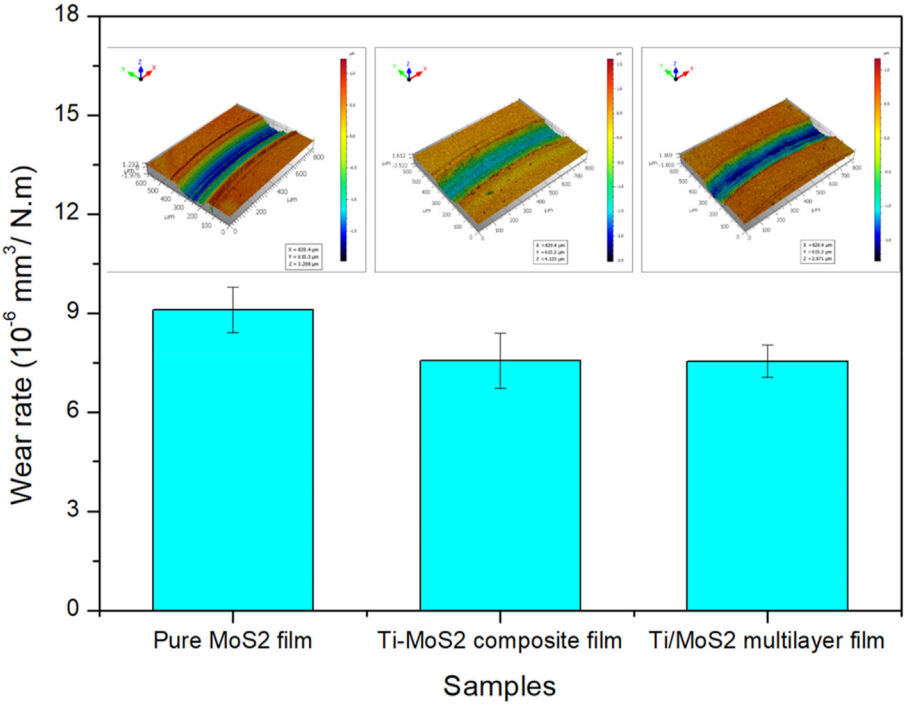

Fig. 8 – The specific wear rate of the three as-deposited MoS_2-based film in NaCl solution, the inset is the corresponding 3D morphologies of the wear tracks.

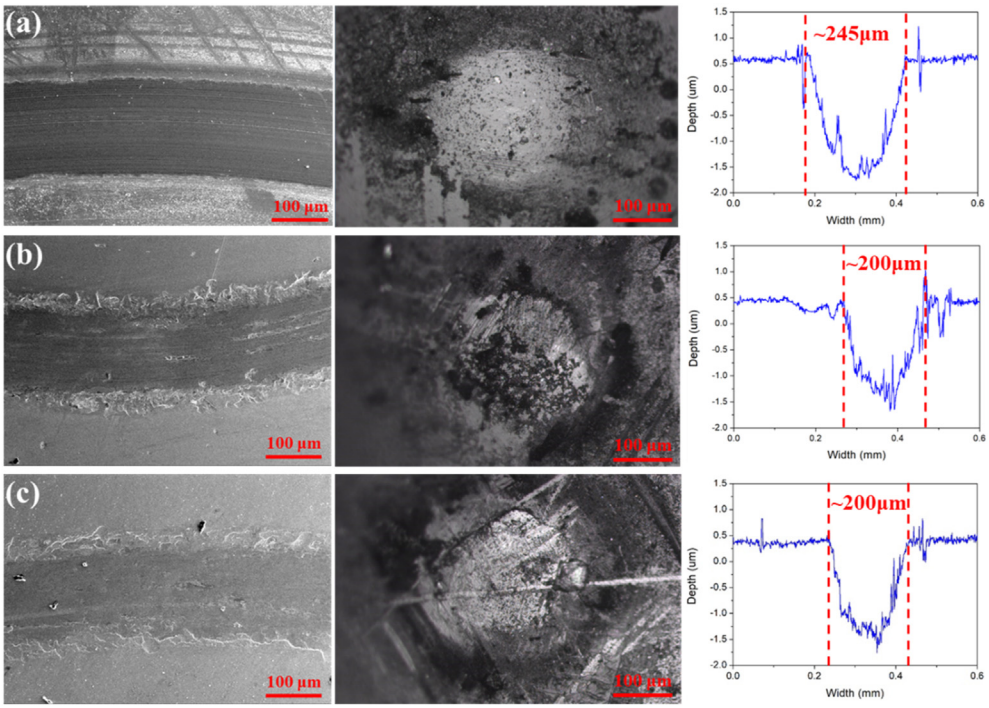

Fig. 9 – The wear track of the films surface, the corresponding wear scar on the mating balls, and the cross-sectional profiles of the wear track perpendicular to the friction direction of the films: (a) pure MoS_2 film, (b) Ti–MoS_2 composite film, and (c) Ti/MoS_2 multilayer film.

[51,52]. As shown in Table 2, both of the Ti-modified MoS_2-based films present higher R_p than that of pure MoS_2 film. The ranking of R_p is Ti/MoS_2 multilayer film > Ti–MoS_2 composite film > pure MoS_2 film, suggesting the best corrosion protection for the multilayer film.

The effect of friction on the corrosion resistance of the three MoS_2-based film in artificial seawater solution was investigated by recoding the polarization curves after friction tests. The results are shown in Fig. 10b and corresponding electrochemical parameters are summarized in Table 2. Compared with the polarization curves in Fig. 10a, it can be seen that the corrosion potential becomes more negative after the friction tests for all of the three MoS_2-based films. Likewise, the I_{corr} after the friction tests in Table 2 also show higher values than that obtained without friction, indicating reduced corrosion resistance. However, the variation of the E_{corr} and I_{corr} before and after friction for the pure MoS_2 film is greater than that of Ti–MoS_2 composite film and Ti/MoS_2 multilayer film, suggesting that the Ti-modified MoS_2 films could provide more effective corrosion protection under tribological conditions.

To better understand the electrochemical properties of the MoS_2-based films, the measured electrochemical impedence spectroscopy (EIS) before and after friction and the fitting results are shown in Fig. 11. The fitted equivalent circuit is shown as an inset in Fig. 11a. The Nyquist plots (Fig. 11a) reveal different behavior for the pure MoS_2 film, Ti–MoS_2 composite film and Ti/MoS_2 multilayer film, with both Ti-modified MoS_2-based films exhibiting higher values of imaginary and real components, suggesting higher capacitance of the Ti-modified MoS_2 films [53]. Compared to the Ti–MoS_2 composite film, the Ti/MoS_2 multilayer film showed higher

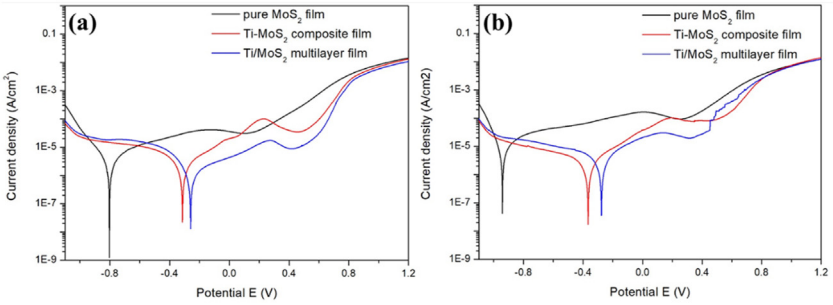

Fig. 10 – Polarization curves of the three as-deposited MoS_2-based film: (a) before friction, (b) after friction.

Table 2 – Electrochemical parameters from polarization curves of the three films before and after friction.

Samples	Pure MoS_2 film		Ti–MoS_2 composite film		Ti/MoS_2 multilayer film	
	before	after	before	after	before	after
E_{corr} (V)	−0.81	−0.94	−0.31	−0.37	−0.26	−0.35
I_{corr} (A/cm^2)	3.77×10^{-6}	7.88×10^{-6}	2.54×10^{-6}	2.58×10^{-6}	1.46×10^{-6}	2.76×10^{-6}
b_a (V/dec)	3.88	4.01	4.32	4.79	3.03	5.04
b_c (V/dec)	6.41	10.75	4.47	3.63	6.28	2.89
R_p (Ω)	2.78×10^5	1.60×10^5	3.76×10^5	3.53×10^5	6.08×10^5	2.89×10^5

radius of the capacitance arcs, which means the best charge transfer resistance to prevent the penetration of corrosive media [49]. The Bode plots also showed a difference between the individual samples. The low-frequency impedance modulus was about 323 kΩ cm^2, 568 kΩ cm^2 and 980 kΩ cm^2 for pure MoS_2 film, Ti–MoS_2 composite film and Ti/MoS_2 multilayer film, respectively, indicating the best corrosion resistance of the multilayer film among the three films [28]. Besides, the range of the phase angle at low and medium frequency is in the order of Ti/MoS_2 multilayer film > Ti–MoS_2 composite film > pure MoS_2 film, confirming the better anti-corrosion ability of the Ti-modified MoS_2 films due to their more uniform and compact microstructure. Fig. 11(c and d) shows the Nyquist and Bode plots of the three MoS_2-based films after friction. Consistent with the results of polarization curves, the capacitance arcs radii, impedance modulus and phase angle of the three films after friction decreased in varying degrees compared with those before friction, indicating decreased reduction in corrosion protection of the films.

The corrosion resistance of protective films is related to their microstructure, composition and wettability behavior [50,54,55]. In general, the better the film hydrophobicity, the better the corrosion resistance. For example, *Li* et al. [50] prepared a superamphiphobic MoS_2 film on steel substrates, exhibiting long-term and stable anti-corrosion property. Interestingly, the WCA in Fig. 6 decreased significantly with the introduction of Ti element, while the corrosion resistance exhibited opposite trend. The main reason for this contradictory result may be attributed to the different microstructure of the films [26,28]. For ideal protective films, the dense microstructure could prevent the penetration of corrosive ions such as chloride ions and oxygen in corrosive medium, so as to provide effective protection to the metal substrate. However, the existence of the micropores and defects is inevitable in the process of film deposition due to the substrate defects and bombardment effect. The amount and size of the pores and pinholes in the film structure determines the migration rate of corrosive ions in the electrolyte. For the pure MoS_2 film, the loose columnar structure provided more diffusion pathways through the micropores and defects in the film structure, resulting in worse corrosion resistance. For the Ti–MoS_2 composite film, the tight nanocrystalline/amorphous composite structure could not only reduce the penetration of corrosive ions, but also capture the transferred electron between the substrate and the electrolyte according to the preferential reaction of metal Ti. The better anti-corrosion property of Ti/MoS_2 multilayer film should be

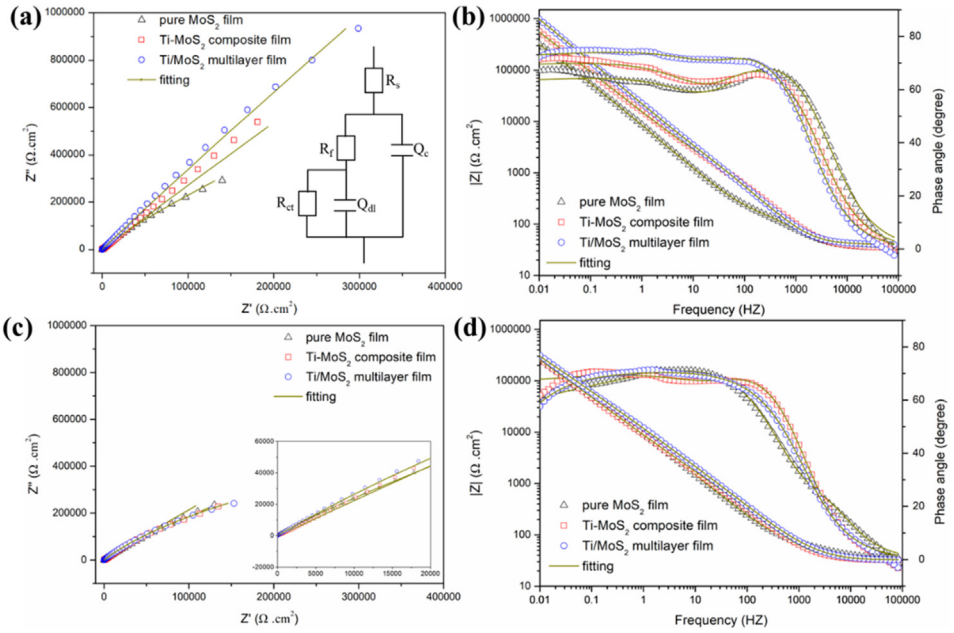

Fig. 11 – EIS behavior of the three as-deposited MoS_2-based film: (a, b) Nyquist plots and Bode plots before friction, (c, d) Nyquist plots and Bode plots after friction.

attributed to the multi-interfaces between the alternating nanostructure. The presence of interfaces can serve as an effective barrier to keep media away from the substrate by reducing the defects throughout film thickness and extending the diffusion path of corrosive ions, thus proving better corrosion protection for the stainless substrate [16,28].

Furthermore, the high corrosion resistance of the Ti-modified MoS_2 films could attributed to the formation of a compact passivated oxide layer on the top of the films [54]. Due to the incorporation of Ti in the film structure it is expected to produce passive film on their surfaces when exposed in NaCl solution. When the normal load is applied, the mechanical interaction would lead to the destruction of the passivation film on the film surfaces [51,54]. In this case, the corrosion resistance of the films is attributed to two parts of the exposed surface, including the passive area outside the track and the active area inside the wear track. The decreased anti-corrosion properties for all of three MoS_2-based films after the friction tests should be ascribed to the reactivation of the wear track due to the sliding effect. For the Ti–MoS_2 composite film and Ti/MoS_2 multilayer film, the repassivation of the friction area reduces the influence of friction on their corrosion properties. Otherwise, the size of the active area should also be considered to account for differences in corrosion properties of the three MoS_2 films after friction. The wider wear trace (Fig. 9) for pure MoS_2 film, corresponding to larger activation area, results in lower corrosion resistance of the total exposed surface.

4. Conclusion

Ti–MoS_2 composite film and Ti/MoS_2 multilayer film were deposited on 304 stainless steel to explore their potential for applications in marine environment by using closed-field unbalanced magnetron sputtering system. The relationship between microstructure, wettability and mechanical properties on their tribological and corrosion performance in 3.5 wt% NaCl solution was investigated as a comparison with pure MoS_2 film. The incorporation of Ti results in a change in the film structure from columnar crystalline to amorphous, which is associated with a reduction of defects and micropores in the Ti–MoS_2 composite and Ti/MoS_2 multilayer films. The higher density and decreased surface roughness of Ti-modified MoS_2 films result in the enhancement of mechanical properties and weakness of the hydrophobic performance, which is responsible for the lower friction coefficient and wear rate compared to the pure MoS_2 film in NaCl solution. However, the strong deviation of elastoplastic properties between the substrate and Ti-modified MoS_2-based films leads to the exfoliation of films at the edge of the wear track, while severe abrasive wear occurred on the surface of pure MoS_2 film. The measured potentiodynamic polarization curves and electrochemical impedance spectroscopy indicate the more effective protection of Ti/MoS_2 multilayer film followed by the Ti–MoS_2 composite film due to the improved compactness and the presence of surface oxide film. The mechanical interaction during the sliding friction would activate the wear track area, resulting in the worse corrosion resistance after friction. The repassivation of the Ti-modified MoS_2 films could effectively reduce the negative effects. Overall, the better tribological and corrosion behavior of Ti–MoS_2 composite film and Ti/MoS_2 multilayer film in simulated seawater indicate potential development for applications as protective films in aggressive corrosive environments.

Declaration of Competing Interest

The authors declare that they have no known competing financial interests or personal relationships that could have appeared to influence the work reported in this paper.

Acknowledgments

The authors gratefully acknowledge the financial support from the Fundamental Research Funds for the Central Universities, China (Grant No: B220202037), the Natural Science Foundation of Jiangsu Province of China (BK20210374), and the Doctoral Program of Entrepreneurship and Innovation of Jiangsu Province (JSSCBS20210254).

REFERENCES

[1] Ye Y, Wang Y, Ma X, Zhang D, Wang L, Li X. Tribocorrosion behaviors of multilayer PVD DLC coated 304L stainless steel in seawater. Diam Relat Mater 2017;79:70–8.
[2] Cao S, Mischler S. Modeling tribocorrosion of passive metals -A review. Curr Opin Solid State Mater Sci 2018;22:127–41.
[3] Ren P, Meng H, Xia Q, Zhu Z, He M. Influence of seawater depth and electrode potential on the tribocorrosion of Ti6Al4V alloy under the simulated deep-sea environment by in-situ electrochemical technique. Corrosion Sci 2021;180:109185.
[4] López-Ortega A, Bayón R, Arana JL, Arredondo A, Igartua A. Influence of temperature on the corrosion and tribocorrosion behaviour of high-strength low-alloy steels used in offshore applications. Tribol Int 2018;121:341–52.
[5] Xie Z, Chen T, Chen Q, Yang Q, Tan S, Wang Y, et al. Tribocorrosion behaviors of AlN/MoS2–phenolic resin duplex coatings on nitrogen implanted magnesium alloys. Surf Coating Technol 2015;266:64–9.
[6] Arslan E, Totik Y, Efeoglu I. The investigation of the tribocorrosion properties of DLC coatings deposited on Ti6Al4V alloys by CFUBMS. Prog Org Coating 2012;74:768–71.
[7] Obadele BA, Lepule ML, Andrews A, Olubambi PA. Tribocorrosion characteristics of laser deposited Ti–Ni–ZrO2 composite coatings on AISI 316 stainless steel. Tribol Int 2014;78:160–7.
[8] Li H, Xie M, Zhang G, Fan X, Li X, Zhu M, et al. Structure and tribological behavior of Pb-Ti/MoS2 nanoscaled multilayer films deposited by magnetron sputtering method. Appl Surf Sci 2018;435:48–54.
[9] Irving BJ, Nicolini P, Polcar T. On the lubricity of transition metal dichalcogenides: an ab initio study. Nanoscale 2017;9:5597–607.
[10] Wei Z, Li B, Xia C, Cui Y, He J, Xia J, et al. Various structures of 2D transition-metal dichalcogenides and their applications. Small Methods 2018;2:1800094.
[11] Zekonyte J, Cavaleiro A, Polcar T. Frictional properties of self-adaptive chromium doped tungsten–sulfur–carbon coatings at nanoscale. Appl Surf Sci 2014;303:381–7.

[12] Choudhary N, Patel MD, Park J, Sirota B, Choi W. Synthesis of large scale MoS2 for electronics and energy applications. J Mater Res 2016;31:824–31.
[13] Vaziriserehk MR, Martini A, Strubbe DA, Baykara MZ. Solid lubrication with MoS2: a review. Lubricants 2019;7:57.
[14] Li Q, Lu H, Cui J, An M, Li DY. Improve the performance of Cr-free passivation film through nanoelectrodeposition for replacement of toxic Cr 6+ passivation in electrogalvanizing process. Surf Coating Technol 2017;324:146–52.
[15] Mouloua D, Kotbi A, Deokar G, Kaja K, El Marssi M, El Khakani MA, et al. Recent progress in the synthesis of MoS2 thin films for sensing, photovoltaic and plasmonic applications: a review. Materials 2021;14:3283.
[16] Sun J, Deng J, Li X, Meng Y, Zhang Y, Zhang L, et al. Preparation and tribological properties of MoS2-based multiple-layer structured films fabricated by electrohydrodynamic jet deposition. Surf Coating Technol 2020;384:125334.
[17] Sun S, Chen J, Wang Y, Wang L, Sun Z. Structural sensitivity of MoS2-based films in solid space lubrication. Surf Eng 2020;36:106–13.
[18] Zeng C, Pu J, Wang H, Zheng S, Wang L, Xue Q. Study on atmospheric tribology performance of MoS2–W films with self-adaption to temperature. Ceram Int 2019;45:15834–42.
[19] Jiang A, Cao X, Wang Z, Ma J, Xiao J, Ma S. Friction performance and corrosion resistance of MoS2/DLC composite films deposited by magnetron sputtering. Results Phys 2021;25:104278.
[20] Xu Y, Xie M, Li Y, Zhang G, Xu X, Fan X, et al. The effect of Si content on the structure and tribological performance of MoS2/Si coatings. Surf Coating Technol 2020;403:126362.
[21] Hudec T, Mikula M, Satrapinskyy L, Roch T, Truchlý M, Švec P, et al. Structure, mechanical and tribological properties of Mo-S-N solid lubricant coatings. Appl Surf Sci 2019;486:1–14.
[22] Rodrigues SP, Polcar T, Carvalho S, Cavaleiro A. The wettability and tribological behaviour of thin F-doped WS2 films deposited by magnetron sputtering. Surf Coating Technol 2019;378:125033.
[23] Zhang W, Demydov D, Jahan MP, Mistry K, Erdemir A, Malshe AP. Fundamental understanding of the tribological and thermal behavior of Ag–MoS2 nanoparticle-based multi-component lubricating system. Wear 2012;288:9–16.
[24] Qin X, Ke P, Wang A, Kim KH. Microstructure, mechanical and tribological behaviors of MoS2-Ti composite coatings deposited by a hybrid HIPIMS method. Surf Coating Technol 2013;228:275–81.
[25] Ding X, Zeng XT, He XY, Chen Z. Tribological properties of Cr- and Ti-doped MoS2 composite coatings under different humidity atmosphere. Surf Coating Technol 2010;205:224–31.
[26] Zeng C, Pu J, Wang H, Zheng S, Chen R. Influence of microstructure on tribological properties and corrosion resistance of MoS2/WS2 films. Ceram Int 2020;46:13774–83.
[27] Ren S, Shang K, Cui M, Wang L, Pu J, Yi P. Structural design of MoS2-based coatings toward high humidity and wide temperature. J Mater Sci 2019;54:11889–902.
[28] Shang K, Zheng S, Ren S, Pu J, He D, Liu S. Improving the tribological and corrosive properties of MoS2-based coatings by dual-doping and multilayer construction. Appl Surf Sci 2018;437:233–44.
[29] Wang Y, Li J, Wang L, Chen J, Xue Q. Tribological performances of graphite-like carbon films coupled to different ceramics in ambient air and water. Tribol Trans 2013;56:333–41.
[30] Lince JR, Carre DJ, FleIischauer PD. Effects of argon ion bombardment on the basal plane surface of MoS2. Lamhmuir 1986;2:805–8.
[31] Cao H, De Hosson JTM, Pei Y. Effect of carbon concentration and argon flow rate on the microstructure and triboperformance of magnetron sputtered WS2/a-C coatings. Surf Coating Technol 2017;332:142–52.
[32] Lince JR, Hilton MR, Bommannavar AS. Metal incorporation in sputter-deposited MoS_2 films studied by extended x-ray absorption fine structure. J Mater Res 1995;10:2091–105.
[33] Moser J, Lévy F. Growth mechanisms and near-interface structure in relation to orientation of MoS_2 sputtered thin films. J Mater Res 1992;7:734–40.
[34] Gu L, Ke P, Zou Y, Li X, Wang A. Amorphous self-lubricant MoS2-C sputtered coating with high hardness. Appl Surf Sci 2015;331:66–71.
[35] Bertoti I, Mohai M, Renevier NM, Szilagyi E. XPS investigation of ion beam treated MoS sub 2 -Ti composite coatings. Surf Coating Technol 1999;125:173–8.
[36] Shuxian Z, Hall WK, Ertl G, Knözinger H. X-ray photoemission study of oxygen and nitric oxide adsorption on MoS2. J Journal of Catalysis 1986;100:167–75.
[37] Robertson J, Blomdahl D, Islam K, Ismael T, Woody M, Failla J, et al. Rapid-throughput solution-based production of wafer-scale 2D MoS2. Appl Phys Lett 2019;114:163102.
[38] Gao B, Du X, Li Y, Song Z. Wettability transition of Ni3B4-doped MoS2 for hydrogen evolution reaction by magnetron sputtering. Appl Surf Sci 2020;510:145368.
[39] Dong D, Jiang B, Li H, Du Y, Yang C. Effect of graphite target power density on tribological properties of graphite-like carbon films. Appl Surf Sci 2018;439:900–9.
[40] Yan M, Wang X, Zhang S, Zhang S, Sui X, Li W, et al. Friction and wear properties of GLC and DLC coatings under ionic liquid lubrication. Tribol Int 2020;143:106067.
[41] Shi X, Shi Y, Chen J, Liskiewicz TW, Beake BD, Zhou Z, et al. Influence of gradient interlayer thickness on corrosion and tribological behavior of Ti-containing multilayer graphite-like carbon films. Wear 2022;488–489:204177.
[42] Musil J, Kunc F, Zeman H, Poláková H. Relationships between hardness, Young's modulus and elastic recovery in hard nanocomposite coatings. Surf Coating Technol 2002;154:304–13.
[43] Tyagi R, Das AK, Mandal A. Formation of superhydrophobic surface with enhanced hardness and wear resistance by electrical discharge coating process. Tribol Int 2021;157:106897.
[44] Singh B, Ali N, Chakravorty A, Sulania I, Ghosh S, Kabiraj D. Wetting behavior of MoS2 thin films. Mater Res Express 2019;6:96424.
[45] Zhao G, Xue Y, Huang Y, Ye Y, Walsh FC, Chen J, et al. One-step electrodeposition of a self-cleaning and corrosion resistant Ni/WS2superhydrophobic surface. RSC Adv 2016;6:59104–12.
[46] Muratore C, Voevodin AA. Control of molybdenum disulfide basal plane orientation during coating growth in pulsed magnetron sputtering discharges. Thin Solid Films 2009;517:5605–10.
[47] Cai JB, Wang XL, Bai WQ, Zhao XY, Wang TQ, Tu JP. Bias-graded deposition and tribological properties of Ti-contained a-C gradient composite film on Ti6Al4V alloy. Appl Surf Sci 2013;279:450–7.
[48] Kim H, La J, Kim K, Lee S. The effects of the H/E ratio of various Cr–N interlayers on the adhesion strength of CrZrN coatings on tungsten carbide substrates. Surf Coating Technol 2015;284:230–4.
[49] Liu G, Zhou SG, Li QF, Wang C, Zhang JW, Liu JP. Effect of MoS_2 on tribological properties and corrosion resistance of MoS_2/a-C:H films fabricated via reactive magnetron sputtering technology. Mater Res Express 2019;6.

[50] Li Z, Hui S, Yang J, Hua Y. A facile strategy for the fabrication of superamphiphobic MoS2 film on steel substrates with excellent anti-corrosion property. Mater Lett 2018;229:336–9.
[51] Cao L, Liu J, Wan Y, Pu J. Corrosion and tribocorrosion behavior of W doped DLC coating in artificial seawater. Diam Relat Mater 2020;109:108019.
[52] Elsener B, Rota A, Böhni H. Impedance study on the corrosion of PVD and CVD titanium nitride coatings. Mater Sci Forum 1991;44–45:29–38.
[53] Bueno AHS, Solis J, Zhao H, Wang C, Simões TA, Bryant M, et al. Tribocorrosion evaluation of hydrogenated and silicon DLC coatings on carbon steel for use in valves, pistons and pumps in oil and gas industry. Wear 2018;394–395:60–70.
[54] Bayón R, Igartua A, González JJ, Ruiz De Gopegui U. Influence of the carbon content on the corrosion and tribocorrosion performance of Ti-DLC coatings for biomedical alloys. Tribol Int 2015;88:115–25.
[55] Khun NW, Liu E, Zeng XT. Corrosion behavior of nitrogen doped diamond-like carbon thin films in NaCl solutions. Corrosion Sci 2009;51:2158–64.